Chem. Senses 29: 365–379, 2004 DOI: 10.1093/chemse/bjh033

Effect of Anatomy on Human Nasal Air Flow and Odorant Transport Patterns: Implications for Olfaction

Kai Zhao[1], Peter W. Scherer[1], Shoreh A. Hajiloo[1] and Pamela Dalton[2]

[1]Bioengineering Department, University of Pennsylvania, RM 120 Hayden Hall, 3320 Smith Walk, Philadelphia, PA 19104, USA and [2]Monell Chemical Senses Center, 3500 Market St, Philadelphia, PA 19104, USA

Correspondence to be sent to: Peter W. Scherer, Bioengineering Department, University of Pennsylvania, RM 120 Hayden Hall, 3320 Smith Walk, Philadelphia, PA 19104, USA. e-mail: scherer@seas.upenn.edu

Abstract

Recent studies that have compared CT or MRI images of an individual's nasal anatomy and measures of their olfactory sensitivity have found a correlation between specific anatomical areas and performance on olfactory assessments. Using computational fluid dynamics (CFD) techniques, we have developed a method to quickly (<few days) convert nasal CT scans from an individual patient into an anatomically accurate 3-D numerical nasal model that can be used to predict airflow and odorant transport, which may ultimately determine olfactory sensitivity. The 3-D model can be also be rapidly modified to depict various anatomical deviations, such as polyps and their removal, that may alter nasal airflow and impair olfactory ability. To evaluate the degree to which variations in critical nasal areas such as the olfactory slit and nasal valve can alter airflow and odorant transport, inspiratory and expiratory airflow with odorants were simulated using numerical finite volume methods. Results suggest that anatomical changes in the olfactory region (upper meatus below the cribriform plate) and the nasal valve region will strongly affect airflow patterns and odorant transport through the olfactory region, with subsequent effects on olfactory function. The ability to model odorant transport through individualized models of the nasal passages holds promise for relating anatomical deviations to generalized or selective disturbances in olfactory perception and may provide important guidance for treatments for nasal-sinus disease, occupational rhinitis and surgical interventions that seek to optimize airflow and improve deficient olfactory function.

Key words: finite element model, human nasal cavity, nasal deformation, nasal fluid mechanics, olfactory stimulus, peri-receptor

Introduction

All physiological functions of the nose start with air flow. As the structure that provides access of ambient air to the lower respiratory tract, the nose functions to filter, warm and humidify the inspired air flowing through it (Proctor, 1982). This is the first line of respiratory defense that protects the delicate structure of the lower respiratory system. Odor perception, another key function of the nose starts with the transport of volatile chemical molecules by air flow to the olfactory receptors, which are located on the ciliated olfactory epithelium buried in an aqueous mucus layer (Hornung and Mozell, 1981). Historically in olfactory studies, calculation of the odorant concentration in the ambient air represented the limits of stimulus quantitation. However, knowledge of the detailed air flow patterns in the human nasal cavity and the subsequent quantity of odorant transport to the olfactory receptor cites appear essential to a complete understanding of human olfaction.

Due to the protected location of the human olfactory epithelium, it has been estimated that only 10% of inhaled air actually reaches the olfactory region during a normal resting breath (Hahn *et al.*, 1993). Not surprisingly, conditions that impair this air flow, such as a deviated septum, nasal inflammation, congestion or polyps, may have significant effects on olfactory perception, as shown in recent clinical studies (Wolfensberger and Hummel, 2002). Studies that have compared CT or MRI images of an individual's nasal anatomy and measures of their olfactory sensitivity have also found a correlation between the airway volumes of specific anatomical regions and performance on olfactory function (Leopold, 1988; Hornung *et al.*, 2001; Damm *et al.*, 2002). Thus, the observed variation in sensitivity, both across individuals and across time, may result from alterations in air flow pattern and odorant transport in the nasal cavity due to anatomical differences in certain critical areas. There is therefore a need to develop a model that can predict details and differences in human nasal cavity air flow fields and odorant uptake under different anatomical variations or pathological conditions.

Air flow profiles in human nasal cavities have been investigated in the past by a number of researchers using *in vitro* models. The earliest nasal physical models were usually cast from noses of human cadavers (Proetz, 1951; Swift and Proctor, 1977; Girardin *et al.*, 1983; Hornung *et al.*, 1987). Quantitative measurement in these casts was made by visualizing smoke in air flow (Proetz, 1951), using miniature Pitot tubes (Swift and Proctor, 1977), using laser Doppler velocimetry (Girardin *et al.*, 1983) and using radioactive tracers (Hornung *et al.*, 1987). To increase spatial resolution and accuracy in measurement, enlarged models of the nasal cavity based on coronal MRI and CAT scans have also been constructed (Hahn *et al.*, 1993; Schreck *et al.*, 1993). Hahn *et al.* (1993) constructed an anatomically accurate, 20× enlarged scale physical model of the right human nasal cavity from coronal CAT scan images. Velocities for inspiratory and expiratory flows under laminar and turbulent conditions were measured using a hot-film anemometer. Although these studies provided valuable descriptive and quantitative information on air flow patterns in the nasal passages, the methods employed were time consuming and thus, limited the number of individuals who could be studied.

Numerical modeling of air flow and odorant transport using accurate nasal geometry is now possible due to the availability of commercial software. Using computational fluid dynamics (CFD) simulation, Keyhani *et al.* (1995, 1997) were the first to examine air flow and odorant transport through one side of the human nose in an anatomically accurate 3-D finite element model that was constructed from coronal CT scans. Their numerical results were validated by comparison with detailed experimental measurements from Hahn's study (Hahn *et al.*, 1993, 1994). Subramaniam *et al.* (1999) presented a similar model constructed from MRI scans that include both sides of the human nasal passages and also the posterior nasal airway and nasopharynx. Martonen *et al.* (2002) constructed a three-dimensional (3-D) physiologically realistic computer model of the human upper-respiratory tract that includes both nasal cavities. The computer representation evolved from cross sectional slices of a silicone rubber impression of a medical school teaching model of the human head and throat.

Despite these advances in numerical modeling, these efforts have also suffered from limitations, due to the difficulty in producing and/or altering numerical meshes from nasal CT or MRI scans. It is also a time consuming process that can take from a few months to 1 year in generating and refining a numerical mesh.

Using CFD techniques and the aid of two commercial software packages, ICEM® (ICEM-CFD Engineering Inc., Berkeley, CA) and AMIRA® (TGS Inc., San Diego, CA) we have developed a method to quickly convert nasal CT scans from an individual patient into an anatomically accurate 3-D numerical nasal model that can be used to predict air flow and odorant transport, which may ultimately determine olfactory sensitivity. This 3-D model can be also be rapidly modified to depict various anatomical deviations, such as polyps and their surgical removal, that may alter nasal air flow and impair olfactory ability. The biggest advance of our technique over previous numerical modeling attempts is that we were able to achieve CFD simulation results from original CT images within a few days, which enables us to model air flow patterns through individualized models of nasal passages and holds clinical promise for relating anatomical deviations to generalized or selective disturbances in olfactory perception.

In this study, one such nasal model that includes both sides of the nasal cavity and the nasopharynx (see Figures 1 and 2) was constructed from 1 mm axial nasal CT scans of an adult female human subject without administration of nasal decongestant. Modifications to this model were made in two specific regions—the nasal valve region and the olfactory region as suggested by previous studies (Leopold, 1988; Hornung *et al.*, 2001; Damm *et al.*, 2002). CFD techniques were then used to accurately simulate laminar nasal air flow and odorant transport in the nasal cavities before and after modification.

Materials and methods

Image analysis and mesh generation

One millimeter axial CT images of the subject were obtained from the radiology department at Thomas Jefferson Hospital (Philadelphia, PA) with a resolution of 512 × 512 pixels per image and a pixel size of 0.3906 × 0.3906 mm. These images were read into the AMIRA® software as a 3-D volumetric image stack, which can be used to generate views of the same 3-D volume from different axes (coronal, lateral, etc.). We found that the coronal view aided with axial and lateral views could best illustrate nasal structure. With the assistance of a radiologist and a surgeon familiar with nasal CT scans and anatomy, the interface between the nasal mucosa and air in the nasal cavity was delineated using an Image segmentation toolbox. Different segmentation schemes available in AMIRA®, including Threshold, Magic Wand, Contour and Snakes, were applied in combination to achieve the best separation of air space from soft tissue.

After necessary smoothing and artifact correction, AMIRA® automatically generates a 3-D surface (Figure 1) that encompasses the nasal airway and outputs it into a STL surface format file. A second commercial software package, ICEM® was then used to fill up the air space with tetrahedral elements. The scheme applied by the ICEM®

software can automatically generate elements over an order of magnitude size range when necessary in complicated or narrow nasal regions to enable the capture of geometric features required to produce similar numerical accuracy in all regions. The mesh was further refined and optimized to ensure good numerical performance. Mesh quality criteria are automatically enforced on all elements including: (i) a correct topology and (ii) an aspect ratio (ratio of shortest to longest edge) >0.3. In addition, a four-layer prism layer consisting of tight and orderly hybrid tetrehedral/pentahedral elements was generated near the boundary surface (Figure 2) to ensure capturing of the rapid near wall changes in air velocity and odorant concentration profile. Any accurate simulation of a surface derivative value, such as odorant flux (derivative of concentration) or fluid shear stress (derivative of velocity) is dependent on such dense grids close to the wall. We have found that a tetrahedral mesh model without the wall prism layer is not capable of providing accurate and consistent numerical information.

The final nasal cavity mesh contains 1.77 million hybrid finite elements. Computation was also carried out using a mesh with more than double the number of nodes to check for grid-independent convergence of the results. The results indicate that the original nodal density in the mesh is sufficient for the computations in the nasal cavity models we have investigated.

Perturbation of nasal anatomy

Several studies (Leopold, 1988; Damm *et al.*, 2002) have quantitatively investigated correlation of human olfactory function and nasal volumetrics in normal subjects and hyposmic patients. Based on these findings, we artificially obstructed or enlarged two nasal regions that appear to be correlated with odor perception in healthy and hyposmic subjects: (i) the olfactory region (slit) or the segment in the upper meatus below the cribriform plate and (ii) the nasal valve region. The purpose of such airway anatomical perturbation was to investigate how local anatomical differences at critical location that was result of baseline anatomical variations within population or of clinical conditions (polyps growth, etc.) could influence overall and local air flow and odorant transport patterns.

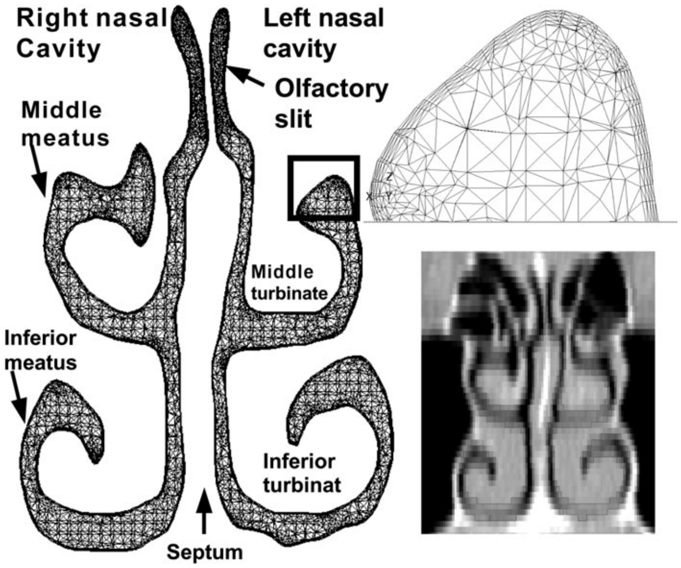

Figure 2 Frontal view (looking into subject's face) of a coronal section of the nasal model (left) and its corresponding CT image (right bottom). The whole model consists of 1.7 million tetrahydral elements. In a close-up view (right top), layers of small and fine elements along the wall can be seen that will capture the rapid near wall changes of air velocity and odorant concentration, which are essential for accurate numerical simulations.

Prior to this investigation, once a numerical mesh was constructed, it was virtually unchangeable, which is the main obstacle that has hindered past efforts to study the relationship between nasal anatomy and nasal air flow. Currently, we can modify original nasal geometry starting at the CT image level. In the regions of interest, we reduced (almost by half) or widened (almost doubled) the airway width of the original CT images and then fed the modified CT images through the same process to output a new nasal airway model. The quick turn around of our technique from CT image to numerical mesh (<few days) makes our approach feasible. Figure 3 shows an overlay of the cross section over the same coronal plane of models with various anatomical changes: these include (i) the original, reduced and enlarged olfactory slit width and (ii) the original, reduced and enlarged nasal valve. As can be seen in the CT image of Figure 3b, the left nasal valve airway is initially partially blocked, so we have one change of the model that just removes the blockage in the nasal valve airway (Figure 3b) and another change of the model that further removes the blockage at the tip of the nasal valve. Altogether, we have developed seven versions of the initial nasal airway model of the same subject: two at the olfactory region, four at the nasal valve region and the original model with slightly blocked left nasal valve.

All these models are perfect reproductions of each other at most nasal regions where changes were not made. This outcome demonstrates the consistency of the modeling technique, since each model is generated independently from its own CT image set. The final number of elements and nodes varies slightly among the seven versions of the model, however a thorough inspection concluded that all versions have the same numerical resolution level.

Numerical simulation of air flow and odorant transport

Both inspiratory and expiratory air flow and odorant transport through the nasal cavity models with or without anatomical modifications can be simulated using the commercial CFD software Fluent® (Fluent Inc., USA) on a SUN Blade® 1000 workstation with a single 700 MHz UltraSparc® II cpu and 2GB memory. So far, we have focused on modeling only laminar air flow in the nasal cavity since previous studies (Swift and Proctor, 1977; Hahn *et al.*, 1993; Schreck *et al.*, 1993; Keyhani *et al.*, 1995) have shown that nasal flow is mostly laminar at flow rates up to about twice the resting breathing flow rate. We further simplify the analysis by treating the flow as quasi-steady rather than fully transient, based on the results of previous research (Girardin *et al.*, 1983; Hornung *et al.*, 1987; Hahn *et al.*, 1993; Keyhani *et al.*, 1995) and also on the fact that the Strouhal number value of the system $(\omega L/U) \approx 0.2$, indicating that the quasi-steady approximation is reasonable under normal resting breathing frequency (ω) and flow rate. However, we retain the capacity to model both turbulent and unsteady air flow and odorant transport in the nasal cavity, if future work indicates this is needed. Numerical details of the simulation of rest breathing air flow in the nose models are provided in the Appendix.

The uptake of odorant into the mucosal lining involving absorption, diffusion and removal of odorant molecules can be described to a first approximation by a dimensionless mass transfer parameter at the mucosal wall, K [see the Appendix for detail: equations (A1)–(A4)]. Odorant uptake through the nasal mucosa is also dependent on two other dimensionless parameters: the Reynolds number $Re = UL/\nu$ and the Schmidt number $Sc = D_a/\nu$, in which D_a is the odorant diffusion coefficient in air, ν is the kinematic viscosity of air (1.7894×10^{-2} kg/m·s), U is the airflow velocity and d_{in} is the characteristic length of the nasal cavity. Given a set of Re, Sc and K values, we can calculate odorant mucosal uptake rate at any location. Table 1 list values with references for K, Sc and other related parameters for the three odorants used in this study. Among these odorants, L-carvone has the same Sc value as D-limonene

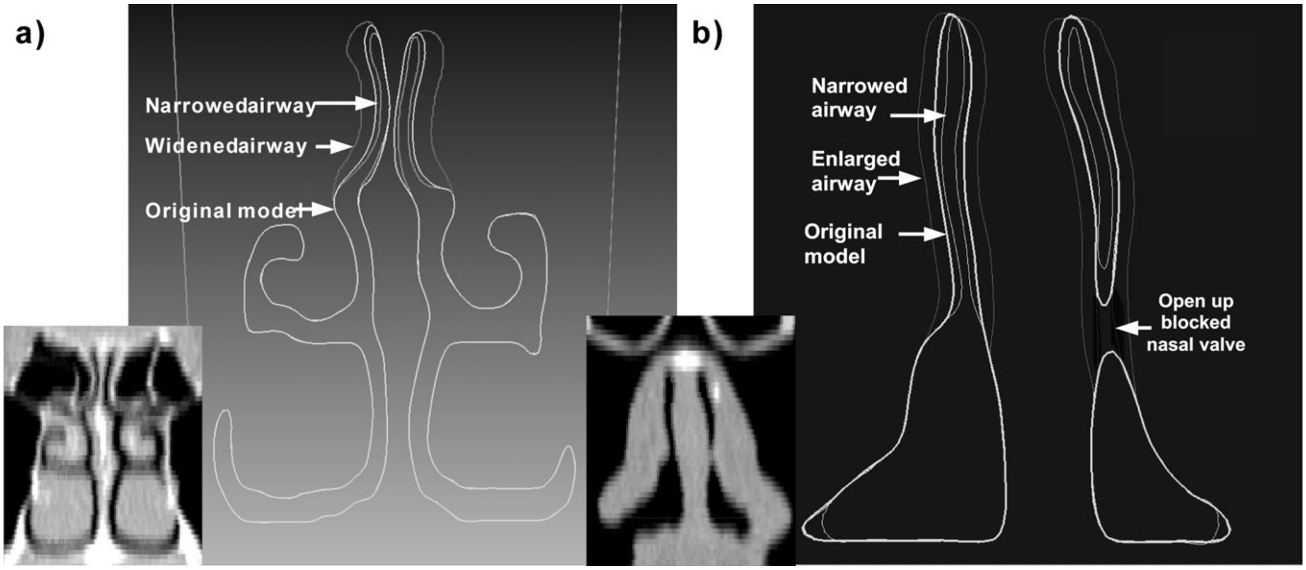

Figure 3 Overlaying of the coronal cross sections of the normal, narrowed and widened nasal airway models with corresponding CT images shown at lower left. **(a)** Anatomical modifications in olfactory slit width; **(b)** modifications in nasal valve region. A small blockage can be clearly seen in the left nasal valve airway on the CT image. Changes in airflow and odorant transport were examined independently by CFD simulation in the altered or normal nasal cavity and the results compared and analyzed.

Figure 1 **(a)** Anatomically accurate numerical nasal model (includes both left and right nasal cavity) constructed from nasal CT scans of a normal adult human female. The nasal air-mucus interface is shown. Inside are ~1.7 million finite elements in which values of air velocity and odorant concentration during flow are calculated. **(b)** Dorsal view of the same nasal cavity model right and left olfactory regions (slits) can be clearly viewed.

Figure 4 Contour plot of velocity magnitude on the coronal planes 6.2 cm from the tip of the external nares. Air flow is simulated by applying atmospheric pressure at the external nares plane and a steady pressure of-15 pascal at the nasopharynx. **(a)** Narrowed olfactory slit. **(b)** Original airway model generated from CT scans. **(c)** Widened olfactory slit. Total airway volume change in each of the modifications $< 5\%$.

Figure 7 Streamlines pattern for steady laminar airflow computed in the right nasal cavity (original model), with no blockage in the nasal airway. Streamlines pattern is smooth.

Figure 13 Computed septal mucosal odorant uptake pattern in the left and right olfactory regions of the original model for two odorants: carvone and D-limonene. Due to its low solubility, D-limonene exhibits a lower but more uniform uptake pattern on the olfactory mucosa, while cavone has a higher uptake rate and gradient. As a result of different local air flow patterns, odorant uptake on the right olfactory mucosa is high in the anterior area and low in the posterior, while on the left it is high in the lower (ventral) part and low in superior (dorsal) part.

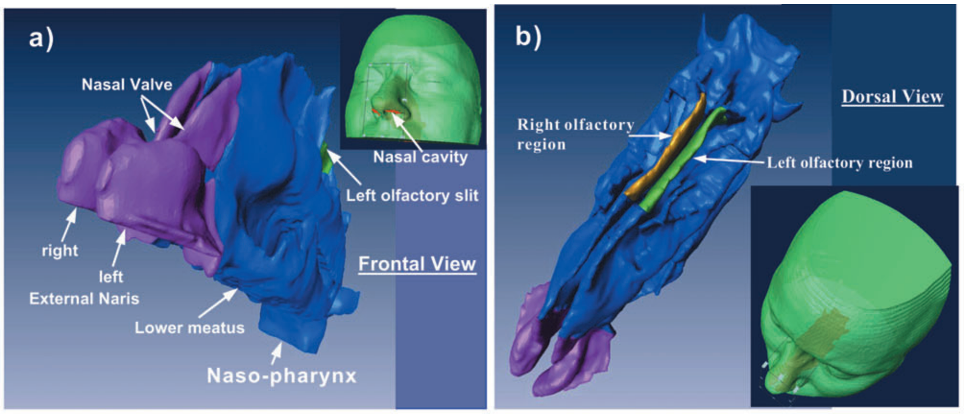

Fig. 1

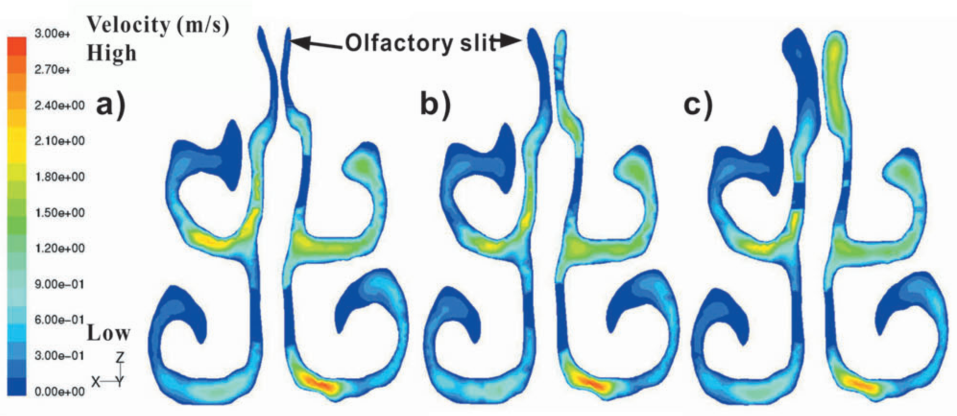

Fig. 4

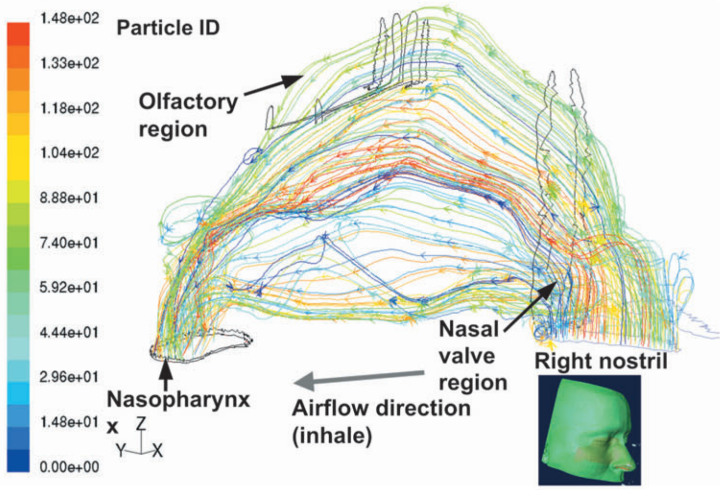

Fig. 7

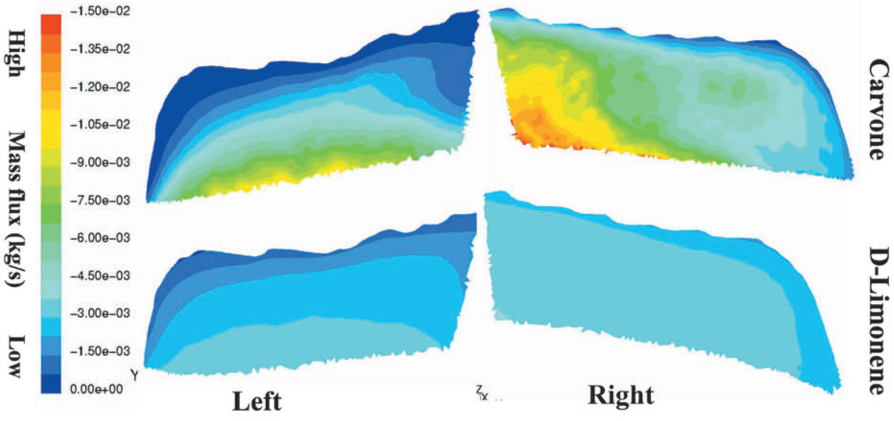

Fig. 13

Table 1 Physical properties for a number of odorants (at 25°C and 1 atm)

Odorant	D_a (cm^2/s)	$D_m \times 10^5$ (cm^2/s)	β (air/mucus)	K^e	*Sc*
L-Carvone	0.062^a	0.69^b	1.30E−04^f	380	2.5
D-Limonene	0.063^a	0.70^b	6.00E−03^f	8.2	2.5
Methanol	0.16^c	1.6^d	1.6E−04^g	270	0.96

D_a = air phase diffusivity; D_m = mucus diffusivity.

[a] Calculated using the Fuller equation (Welty *et al.*, 1976).

[b] Values in water. Calculated using the Wilke–Chang equation (Welty *et al.*, 1976).

[c] Welty *et al.* (1976).

[d] Perry *et al.* (1963).

[e] Calculated using equation (A4) with H_m = 30 µm.

[f] Hornung *et al.* (1980); air/bullfrog nasal mucosa partition coefficients.

[g] Abraham and Weathersby (1994), adjusted from 37 to 25 using an empirical equation given by Abraham *et al.* (1985).

but is much more soluble in mucus (high *K*-value). Methanol is similar in solubility to L-carvone, but much more diffusible (high *Sc*) in air than L-carvone due to its smaller molecular size.

The vestibule of the nose is lined with a stratified squamous epithelium that is moderately keratinized, nonmucous and histologically similar to skin. We therefore assume that the anterior portion of our model, up to 2 mm posterior to the naris (see Figure 1: the region that is pink color coded) is impermeable to odorants with $K = 0$ or zero wall flux. Even if there is a slight uptake in this region, studies have shown that the effect on uptake patterns over the rest of the nasal mucosa is very small (Keyhani *et al.*, 1997).

The olfactory airway (see Figure 1: yellow and green color coded) that lies between the superior turbinate and the septum below the cribriform plate is defined as in previous modeling studies (Hahn *et al.*, 1994; Keyhani *et al.*, 1997) and also taking into account recent human biopsy studies (Feron *et al.*, 1998). It is segmented from the rest of the nasal cavity to monitor the changes in local air flow and odorant transport at this region critical to olfactory function. Since olfactory and respiratory epithelia are virtually indistinguishable (except through histologic methods) and the two types merge into each other without clear-cut distinction, the same wall boundary conditions are applied for both types of epithelium lining. We have, however, applied double the mesh density in the olfactory region to ensure an accurate wall flux simulation at this region.

Results and discussion

Air flow analysis

The computed velocity field in the subject's original nasal cavity model is plotted as constant velocity contours on a coronal plane in Figure 4b. Total air flow rate through both nostrils is 248 ml/s, which is in the lower range of flow rates observed during quiet restful breathing (200–500 ml/s). The right nostril has a higher air flow rate (143 ml/s) than the left side (105 ml/s), which is probably due to nasal cycling (total airway volume in the right nasal cavity is 14% larger than in the left, 12.24 versus 10.75 ml) and the obstruction noted above in the subject's left nasal valve region (see Figure 3b). The distribution of air flow within the nasal passages is generally consistent with that described in previous literature (Hahn *et al.*, 1993; Keyhani *et al.*, 1995). The highest air flow occurs along the nasal floor of the lower meatus while a second peak occurs in the middle meatus close to the septum. The lowest air flow occurs through the superior region of the nasal cavity. Only ~8% of total external nares air flow in the right nasal cavity and 2% in the left actually passes through the olfactory region, which is in the range of previous reports: 5–10% (Stuiver, 1958), 14% (Hahn *et al.*, 1993) and 5% (Kelly *et al.*, 2000). The variation of the fractional air flow rate through the olfactory region reported in the literature and in this study are probably all due to differences in the dimensions of the nasal cavity studied. As we will demonstrate in this study, nasal airflow pattern and olfactory airflow rate are highly sensitive to local anatomic dimensions in certain nasal cavity regions.

We performed a similar flow field analysis on all the other numerical meshes with anatomical perturbations. Figure 5 summarizes air flow rate changes among the three models with modifications in the olfactory region as outlined in the methods section. In Figure 5a, global air flow rates—defined as total air flow rates though nostrils—are plotted against right or left side olfactory region volume. As can be seen from the logarithmic horizontal axis, the olfactory region airway volume was reduced by approximately half and doubled in the two modifications respectively. Although there is a slight increase in global air flow rate, changes are very small, due to the fact that the olfactory region itself is relatively small and at a protected location in the back of the nasal cavity. Volume change in that region is insignificant to the total resistance of the nasal airways: the modifications made in the olfactory region account for only 5% of total airway volume.

In contrast to global air flow however, local air flow through the olfactory region (as shown in Figure 5b) greatly increases as olfactory region airway volume increases. The flow rate goes from 0.56 ml/s on the right side when olfactory region airway is constricted to 28.3 ml/s (50 times greater) when the airway is opened up, suggesting that rather small absolute anatomical volume differences in the olfactory region can lead to large differences in olfactory air flow rate. In other words, a subject who breathes in approximately the same amount of air (Figure 5a) can have up to 50 times greater local air flow (Figure 5b) supplying odorant to his/her olfactory region as a function of local anatomical differences.

Figure 4 compares the contour plot of velocity on the exact same coronal plane of three variations of the model.

Airway size and velocity differences in the olfactory slits are shown. There is also a small global flow redistribution after local airway size is modified.

As with the global flow rates, local flow rate through the olfactory region in the right nasal cavity is consistently higher than through the left side and also more dependent on the local volume changes, which cannot be explained simply by the local airway volume differences. In fact, the anatomic volume of the left olfactory region is consistently larger than on the right side in every version of the model. Streamline analysis of the airflow revealed that this reduced left olfactory region air flow rate is due to the upstream obstruction in the left nasal valve and its effect on the air flow pattern discussed below.

Figure 6 summarizes air flow rate changes among the five models with modifications in the nasal valve region as outlined in the methods section. Computed (i) total air flow rates and (ii) local olfactory region air flow rates are plotted against local airway volume (linear scale) in the nasal valve region of the various modified nasal airway models. Total air flow rate through the left and/or right nostril increases when the nasal valve region airway is expanded. Especially in the left nasal cavity, when the originally slightly blocked nasal valve airway is reopened (version 1–3), the air flow

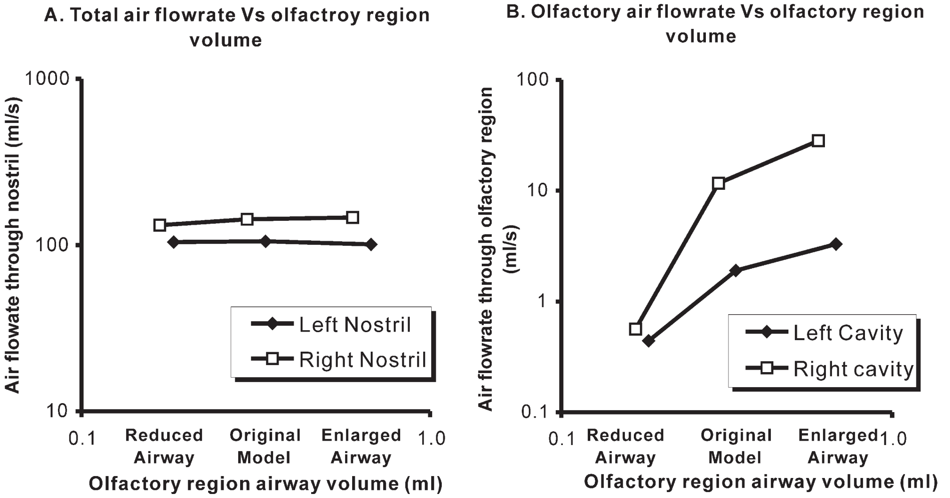

Figure 5 Computed changes in **(a)** total nasal air flow rate and **(b)** local olfactory region air flow rate as a function of widening or narrowing the olfactory slit while keeping all else in the nasal cavity constant. Results show that (a) total nasal airflow rate is little affected by the olfactory airway changes, while (b) local airflow rate through olfactory region is greatly affected. All axes are in logarithmic scale.

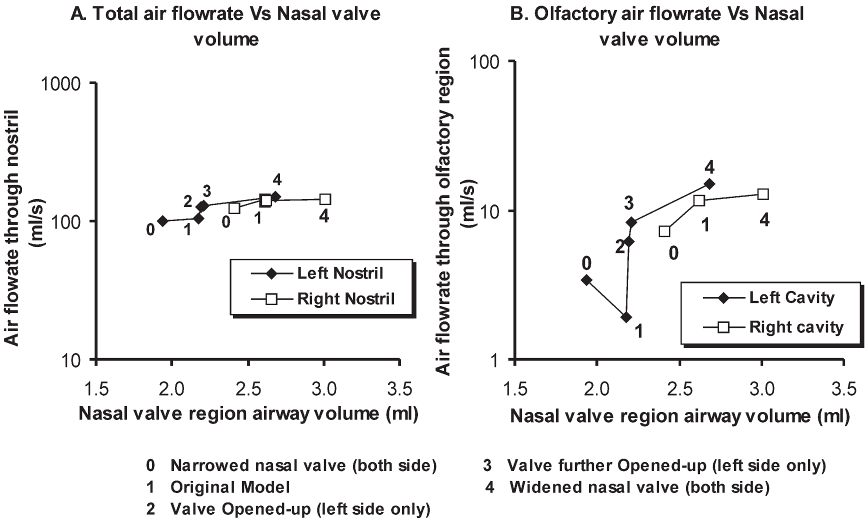

Figure 6 Computed changes in **(a)** total nasal air flow rate and **(b)** local olfactory region air flow rate as a function of various modification in the nasal valve region while keeping all else in the nasal cavity constant. Results show that (a) total nasal airflow rate is affected (largest increase: 23%) by the olfactory airway changes, however not as strongly as (b) local airflow rate through olfactory region (largest increase: 784%).

rate through the left nostril increased significantly (23.1%), even though the airway volume change during the reopening is very small.

Again we observed that the scale of change in global air flow rate was small compared to the local air flow rates through the olfactory region, especially on the left side. Local olfactory air flow rate increased from 1.90 ml/s in the original model to 14.9 ml/s (784% increase) after the originally slightly blocked left nasal valve was opened up and further expanded. The shape of the local flow rate versus nasal valve airway volume curves after the blockage removal also approached an asymptote with the location of the original airway volume again located on the curve at its most sensitive control point (see Figure 6).

As shown in Figure 6, the most dramatic control of nasal air flow was a small blockage in the nasal valve region, where a small (1.45%) reduction of local airway volume can result in an 18.7% decrease in global air flow rate through the nostril and a 76.9% decrease in local olfactory air flow rate. Similarly removal of such a blockage can result in a 23.1% increase in global air flow rate through the nostril and a 334% increase in local air flow rate through the olfactory region. If we apply the modification simultaneously to both local regions of nasal anatomy (i.e. constricting the nasal valve and the olfactory airway or expanding both), we can easily achieve over two orders of magnitude difference in local air flow rate through the olfactory region, while global air flow rate though nostrils changes by a modest 20–30%. There is little doubt that this increase or decrease has significant potential to alter odorant transport to the receptors, and hence olfactory perception.

In Figure 6, both global and olfactory air flow rates in the right nasal cavity of the original model are significantly higher than on the left side. However, we can achieve the same level of ventilation both globally and locally through the olfactory region by expanding both nasal valve airways to a similar level despite other anatomical differences between the left and right nasal cavity. This suggests that the nasal valve is a key controlling region for regulating both global and local nasal air flow through the olfactory region. It literally does act like a 'valve' to the whole nasal ventilation system. Although the contribution of the nasal valve to total nasal air flow was recognized earlier by Haight and Cole (1984), who found that the valve accounts for more than half of the total nasal resistance, the even more important role of the nasal valve in regulating local air flow pattern and olfactory flow distribution had not been known prior to this study. In addition, the olfactory slit remains an important local air flow self-regulator, which can effectively adjust olfactory air flow rates without a large disturbance of air flow elsewhere.

The only data point (point 0, left nasal cavity) in Figure 6b that does not behave in accordance with the model expectations is the one showing that with further narrowing of the original nasal valve in the left nasal cavity, local olfactory air flow surprisingly increases while global flow rate through the left nostril decreases as expected. To better understand this, we studied the detail of the steady flow pattern through both nasal cavities by looking at the streamlines. Figure 7 shows the simulated air flow streamlines in the right nasal cavity of the original model, when neutrally buoyant particles are released on the right external naris plane. Apart from a few re-circulating streams in the nasal vestibule and nasopharynx, there is no flow separation or flow re-circulation in other parts of nasal cavity. Air that flows through a specific region originates at a specific location on the external naris plane. For example, only the air that enters the distal (ventral) tip of the nares reaches the olfactory region. Previous researchers (Masing, 1967; Hahn *et al.*, 1993; Keyhani *et al.*, 1995; Subramaniam *et al.*, 1999; Kelly *et al.*, 2000) have reported a similar nasal flow pattern in their numerical simulations or experiments.

Figure 8 shows a streamline simulation for the left nasal cavity of the original model. The flow pattern, however, is completely different from that previously shown for the right. Air flow starts to separate at the nasal valve close to the blocked region and forms a vortex in the anterior upper part of the nasal airway. A second vortex is formed in the posterior upper part of the nasal cavity close to the olfactory slit, so that local olfactory air flow enters the olfactory region from the bottom and exits from the front (anterior) or back (posterior). These vortices create air mixing and recirculation. For the local air flow through olfactory region, only a portion of the entering flow stream is fresh air containing the ambient concentration of volatile chemicals from the environment. Also with the nasal valve obstructed, it becomes harder to predict from their nares entry point through which nasal region the air streams might flow. An air flow vortex similar to that seen in our left original nasal

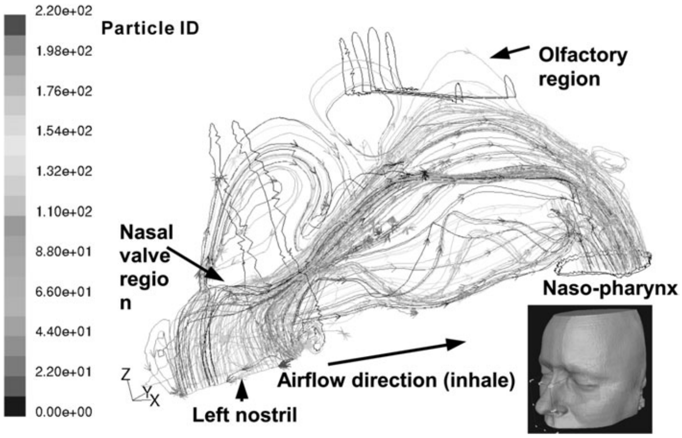

Figure 8 Streamline pattern for steady laminar airflow computed in the left nasal cavity (original model). Compared with Figure 9, streamlines pattern is more complicated with an eddy in the anterior part of nose induced by the small blockage in the left nasal valve region and a second eddy in the posterior upper part of the nose. Formation of these eddies affects local air flow pattern in the olfactory region.

cavity has been described in several prior experimental observations (Swift and Proctor, 1977; Schreck *et al.*, 1993), but only in the present study, can we appreciate how easily the obstructed nasal valve can cause such a vortex. As the small blockage in the left nasal valve was removed (data point 2 in Figure 6b), both vortices in the upper nasal airway disappeared and air flow became smooth and orderly as in the right nasal cavity; correspondingly a sharp increase occurred in left local olfactory air flow.

Figure 9 shows the streamline pattern for the left nasal cavity after further narrowing the original slightly blocked nasal valve. As can be seen, the narrowing of the nasal valve suppresses the frontal air flow vortex and enhances the second vortex near the olfactory slit. This enhanced second vortex is the reason for the increased olfactory local air flow observed in Figure 6b (data point 0, left cavity).

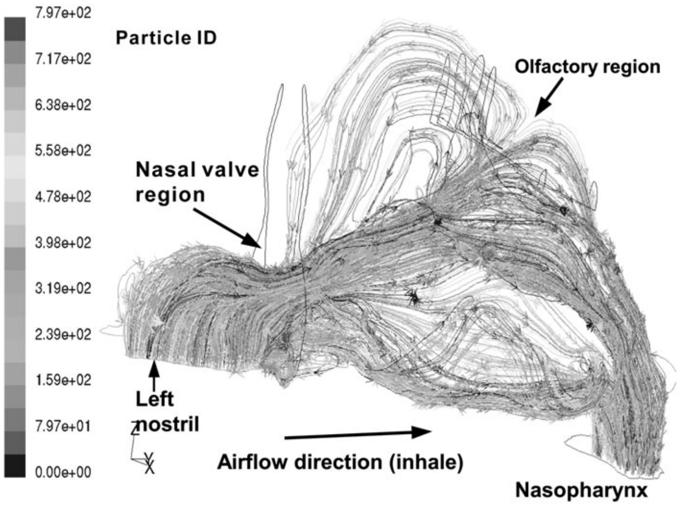

Figure 9 Streamline pattern for steady laminar airflow computed in the left nasal cavity (narrowed nasal valve model). Narrowing the nasal valve airway suppresses the first eddy in the anterior part of the left nasal cavity seen in Figure 10, and enhances the second eddy in the posterior superior part. The very large effect that these small nasal valve anatomical changes can have on streamline patterns is shown.

The above analysis of air flow streamlines shows the complicated dependency and great sensitivity of local olfactory air flow pattern on the anatomy around the nasal valve region. The large variation in the flow patterns observed in the past in various physical models of the human nasal cavity can most likely be traced to the anatomical differences in the noses being studied and especially to the differences in the anterior parts of the nasal cavities (Keyhani *et al.*, 1997). These differences have enormous implications for the sensory functions of the nose—most importantly odor perception.

Numerical rhinomanometry

The pressure-drop/air-flow characteristics (see Figure 10a) was also evaluated in the original nasal model by varying the pressure difference applied between the nostril and the nasopharynx of the original nasal model and computing the changes in air flow during both inhalation and exhalation, similar to what is done mechanically in human rhinomanometry measurements (Pallanch *et al.*, 1985). We can achieve numerical convergence for pressure differences ΔP of up to 80 Pa (0.816 cmH_2O) with a resulting maximum total nasal air flow of ~700 ml/s, or about three times the normal resting breathing rate and towards the onset of turbulence (Hahn *et al.*, 1993). The 'S' shape of the simulated flow versus pressure drop curves resemble experimental rhinomanometry measurements (Figure 10a), which is due to the pressure drop associated with developing laminar velocity boundary layers in the nasal cavity and not to turbulent air flow at flow rates <700 ml/s. Air flow through the right nostril is seen to be significantly higher than through the left nostril during both inhalation and exhalation due to the constriction of the left nasal valve.

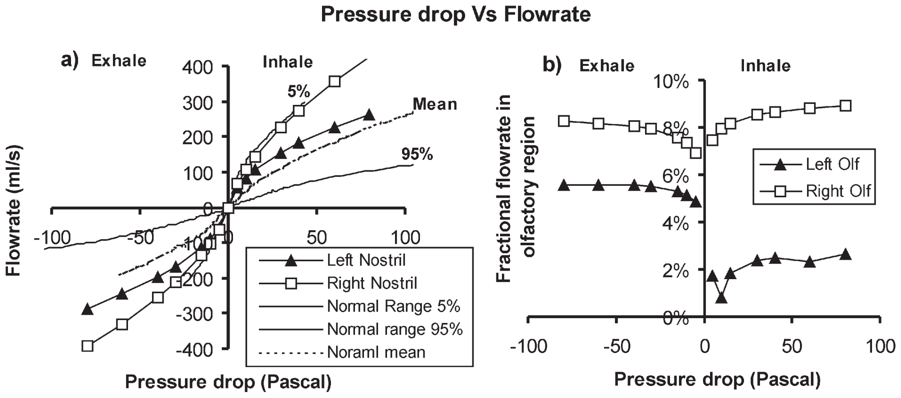

Figure 10 Numerical rhinomanometry: computed **(a)** total air flow and **(b)** fractional local flowrate through olfactory region plotted against the pressure-drop across the whole nasal cavity (between external naris and nasopharynx) for both inhalation and exhalation in the original model. The 'S' shaped curves of the numerical simulations in plot (a) resemble experimental rhinomanaometry measurements and are with the 5–95% range observed among the normal population.

Both curves however are within the 5–95% range observed in the normal population (Pallanch *et al.*, 1985).

In Figure 10b, fractional olfactory air flow rate (local olfactory air flow rate divided by total air flow rate through each nostril) is plotted against air pressure difference across the corresponding nasal cavity model. As can be seen, fractional air flow rate slightly increases as the total air flow rate increases during both inhalation and exhalation. There are slight differences in right olfactory fractional flow rate between inhalation and exhalation, due to the different relative geometrical orientations of the olfactory region to the inlet when flow is reversed. The differences between inhalation and exhalation in the left nasal cavity is more pronounced, where the expiratory flow versus pressure drop curve is significantly higher and smoother than for inhalation. This is due to the constriction of the nasal valve region being downstream from the olfactory region during exhalation. A study of the streamlines in the left nasal cavity during exhalation shows a smooth air flow pattern with no flow separation or re-circulation in the nasal airway. The regulatory effect of the nasal valve on air flow pattern and distribution in the nasal cavity is most pronounced during inhalation when it is at a location upstream to most of the flow. This finding suggests that reported differences between orthonasal and retronasal olfactory sensitivity among some subjects (Pribitkin *et al.*, 2003) can be partly attributed to the different airflow pattern during inhalation and exhalation.

At the lowest pressure-drop point for the left nasal cavity during inhalation (Figure 10b), we saw an abrupt increase in fractional olfactory air flow rate. Streamline computation has revealed that in this low flow rate situation, flow separation and eddy formation due to the slightly blocked left nasal valve is restricted to a local region just beyond the nasal valve and there is no vortex formation or re-circulation in other parts of the nasal cavity. So, another important piece of information is that the formation of air flow separation or vortex is dependent on the air flow rate or more precisely the *Re* number. Air flow separation or vortex formation is more likely to occur and have a bigger influence over downstream air flow pattern at high flow rate with the size, intensity and position of the vortex sporadic dependent on air flow rate. The jagged curve of fractional left olfactory flow rate versus pressure drop during inhalation (Figure 10b) is the result of this flow dependent vortex formation. This is another demonstration of the complexity of nasal air flow and the power of the CFD technique to model the various controlling parameters.

The ability to perform numerical rhinomanometry on any given subject can provide accurate predictions of how nasal resistance will change with modification of nasal cavity anatomy, thus making this technique a promisingly valuable pre-surgical tool. At present, however, numerical rhinomanometry also offers a technique to validate our model by comparing the numerical flow–pressure drop curves to the experimental rhinomanometry curves taken on the same subject.

Nasal odorant transport

The importance of this technique for modeling airflow is matched by its relevance to understanding the process of nasal odorant transport, and thus, odor perception. From the nasal velocity field, the odorant concentration field is determined by solving the un-coupled convection and diffusion equations (A2)–(A4). The mass flux of odorant over the entire nasal surface and particularly over the olfactory mucosa was determined from the wall concentration gradients equation (A6). Figure 11 depicts a plot of the computed fractional uptake of (i) the entire nasal surface and (ii) local olfactory mucosa for the three models with various olfactory slit widths. All the empty symbols and dotted lines are for the left nasal cavity, solid ones are for the right nasal cavity and the three symbols indicates the three odorants. Total whole nose fractional uptake of the three odorants used in our simulation remains about constant for all different models (~72% uptake for L-carvone, 90% for methanol and 22% for D-limonene). Uptake of methanol is greatest since it

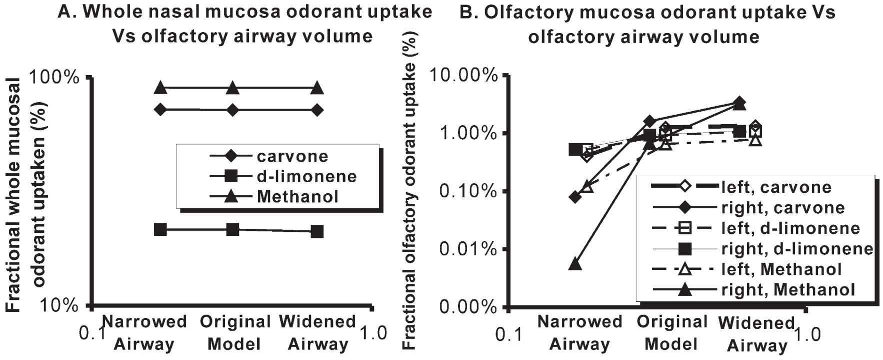

Figure 11 Computed changes in fractional **(a)** whole nasal mucosal odorant uptake and **(b)** local olfactory mucosal odorant uptake as a function of widening or narrowing the olfactory slit while keeping all else in the nasal cavity constant. Results show that (a) whole nasal mucosal odorant uptake is little affected by the olfactory airway size changes, while (b) local olfactory mucosal odorant uptake in the olfactory region is greatly affected, especially for high mucosal soluble and high air diffusable odorants carvone and methanol.

has both high solubility and high air phase diffusivity. Our simulation data generally matches that of (Keyhani *et al.*, 1997) for the same three odorants, taking into account that Keyhani's nasal model included only a right nasal cavity and was truncated before the nasal pharynx. Local fractional uptake over the olfactory mucosa does vary however with olfactory slit width change. We see bigger changes in fractional uptake over the right olfactory mucosa of the different versions of models than over the left due to the larger local air flow rate changes in the right cavity (as shown in Figure 5). The shapes of the olfactory odorant uptake curves generally match the curves observed for olfactory air flow. L-Carvone and methanol also show consistently higher variation than D-limonene. In the case of methanol uptake in the right nasal cavity, the change is over two orders of magnitude. This observation suggests that uptake of odorants with higher mucosal solubility and/or higher air diffusivity is more affected by local air flow pattern and anatomical changes than odorants with lower mucosal solubility and/or lower air diffusivity.

Figure 12 is a plot of the computed fractional uptake of (i) the entire nasal mucosa and (ii) the local olfactory mucosa for the five models with various modifications in the nasal valve region. Total whole nose fractional uptake of the three odorants remains approximately constant for all different models with a slight decrease as the nasal valve is widened. The slight decrease is due to the increased total air flow rate. Higher air flow rate means less time is needed for air to pass through the system and subsequently this reduces time available for odorant to be taken up by the mucosa. This effect is most pronounced for low solubility odorant such as D-limonene. Local fractional uptake over the olfactory mucosa does fluctuate much more dramatically with nasal valve volume changes. The local uptake changes are in general agreement with air flow rate curves in Figure 6 and follow the general conclusion that odorants with higher mucosal solubility and/or higher air phase diffusivity are more likely to be affected by local air flow pattern changes. However, there are a few discrepancies: Figure 6 shows an increase in olfactory airflow from model 1 to 2, while Figure 12 shows a decrease in olfactory odorant uptake of methanol and L-carvone from model 1 to 2. This is because local mucosa uptake is not only dependent on convective transport (local airflow rate), but also on the concentration of the remaining odorant in the local air stream. When the blocked nasal valve region is partially opened from model 1 to 2, even though local olfactory airflow rate increases, the flow pattern results in more odorant uptake upstream in the anterior part of the nose and therefore lowers the concentration of the higher solubility odorant available in the air stream of the olfactory region.

Since the distribution of various types of olfactory receptors on the olfactory mucosa is not uniform, it has been postulated by numerous researchers that the odorant mucosa spatial deposition pattern may be an important determinant of the olfactory perception (Mozell, 1966, 1970; Moulton, 1976; Mozell and Jagodowicz, 1974). Figure 13 shows the mucosal odorant deposition pattern on the septal wall in the left and right olfactory region (defined in Figure 1) of the original model for L-carvone and D-limonene. On the right, uptake of odorant is always high in the anterior part of the region and decreased towards the posterior. On the left however, uptake of odorant is high at the bottom part (ventral) and low at the upper part (dosal) of the olfactory slit. This large difference in odorant deposition pattern is due to the difference in local air flow pattern

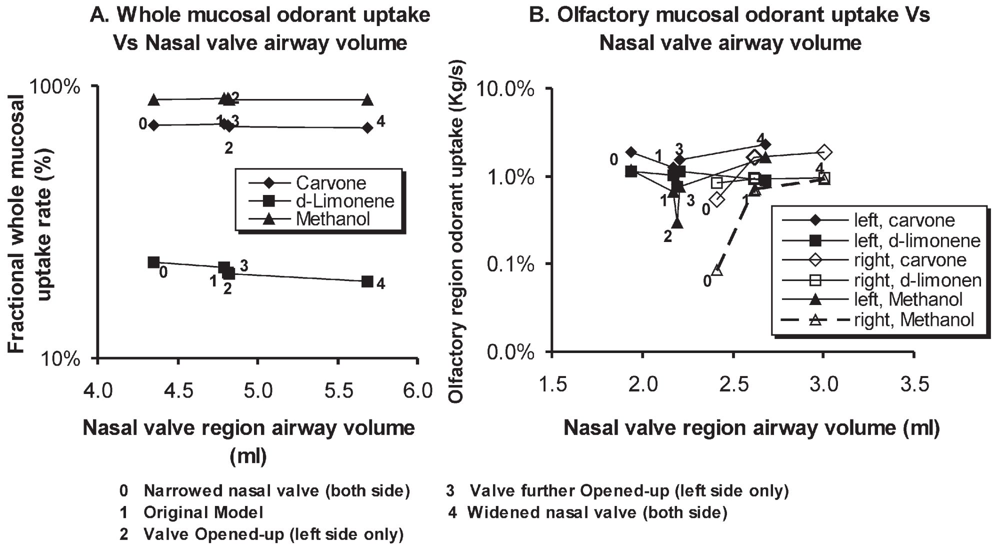

Figure 12 Computed changes in fractional **(a)** whole mucosal odorant uptake and **(b)** local olfactory mucosal uptake as a function of various modifications in the nasal valve region while keeping all else in the nasal cavity constant. Results show that (a) whole mucosal odorant uptake is little affected by the nasal valve changes, while (b) local olfactory mucosa odorant uptake in the olfactory region is greatly affected, especially for high mucosal soluble and high air diffusable odorants.

as discussed previously. The recirculating vortex in the upper posterior part of the left nasal cavity shown in Figure 8 forces air flow to enter the olfactory region from the bottom and exit from the front or back. These simulation results provide additional support to the conclusion that variation in anatomical structures can modulate the olfactory odorant deposition pattern dramatically.

Conclusion

These numerical simulation studies have shown that relatively small changes in the anatomy of nasal cavity at specific locations can induce large changes in the airflow through and the odorant uptake on the olfactory mucosa, a feature that cannot be evaluated using standard rhinometric assays. Also, previous research approaches, using a single cast or model to draw general gross flow features for the general population, would appear to be unsuitable for investigations related to human olfaction, since inter-individual variations in nasal anatomy and even anatomical variations of the same subject at different time frame due to congestion or decongestion can cause substantial variations in nasal air flow and odorant transport pattern. Clinical conditions, such as inflammation, allergy, sinusitis, polyps, etc. can further complicate the analysis.

Results from the current study also signal a warning to investigators in the chemosensory field that controlling global air flow parameters such as breath rate, flow rate and rhinometry measurements may not be sufficient to establish uniform conditions of odorant concentration during olfactory testing. We have demonstrated in the current study that at different anatomical conditions, air flow rate through the olfactory region and odorant uptake rate in olfactory mucosa can possibly differ up to two orders of magnitude, while air flow rates through the nostrils and total cross sectional area remain at a relatively constant level.

Finally, it is interesting to note that anatomical variations can play a different role during inhalation and exhalation, which could be a potential explanation of the observed difference between ortho and retro nasal olfactory sensitivity among some nasal-sinus disease patients.

Our ability to obtain accurate numerical simulations of nasal air flow and odorant transport quickly from individual human nasal CT scans under different conditions indicates that this technique can shed considerable light on the peri-receptor processes involved in olfactory perception and has the potential to become a useful and powerful tool in pre-operative nasal surgery preparation.

Appendix: numerical simulation of air flow and odorant transport

Table A1 Nomenclature

C	Mass concentration of inhaled odorants
C'	Non-dimensional mass concentration of inhaled odorants = C/C_{in}
C_{in}	Mass concentration of ambient odorant at the external naris
C_{m}	Mass concentration of odorant in mucosal layer
D_{a}	Binary diffusion coefficient of inhaled odorants molecules in air
D_{m}	Binary diffusion coefficient of inhaled odorants molecules in mucus
H_{m}	Thickness of the mucus layer
j	Mass surface flux
K	Non-dimensional parameter defining mucosal boundary condition =
n	Unit normal vector to a given surface
P	Air pressure
Re	Reynolds number = Ud_{in}/ν
Sc	Schmidt number = ν/D_{a} in gas phase
u_i	Velocity component
U	Average velocity over a given cross-section
x_i	Position vector
y	Coordinate normal to the nasal epithelium surface
y'	Non-dimensional coordinate normal to the nasal epithelium surface
β	Air/mucus partition coefficient
ν	Kinematic viscosity of air
ω	Breathing frequency
ρ	Density of air

The governing equations (continuity and Navier–Stokes equations) for the incompressible steady air flow through the nose (for nomenclature, see Table A1):

$$\frac{\partial u_i}{\partial x_i} = 0 \tag{A1}$$

$$\rho u_j \frac{\partial u_i}{\partial x_j} = -\frac{\partial P}{\partial x_i} + \mu \frac{\partial^2 u_i}{\partial x_j \partial x_j}$$

are solved by Fluent, using a finite volume scheme (Fluent Inc., 1998). In the equations, P is the pressure, u_i is the velocity vector and x_i is the position vector. The walls of the nasal cavity are assumed to be rigid under normal rest breathing rate and the non-slip condition on the velocity is applied at the mucus–air interface. The air pressure is held constant at 1 atm at both nostrils. For inhalation, a negative pressure of –15 Pa compared to atmosphere is applied at the nasopharynx (see Figure 1) as the driving force of air flow through the nose, while a positive pressure of 15 Pa is applied for exhalation.

Odorant transport and uptake or removal in the nasal cavity is then simulated based on the computed steady air flow field, under the assumption that the effect of odorant concentration on the velocity field is negligible for the typical low odorant concentration inhaled through nose.

The uncoupled governing equation of odorant convection and diffusion in the air phase:

$$u_i \frac{\partial C'}{\partial x_i} = D_a \frac{\partial^2 C'}{\partial x_i \partial x_i} \quad \text{(A2)}$$

is also solved by Fluent with appropriate wall boundary conditions (A3), where $C' = C/C_{\text{in}}$ is the normalized odorant concentration, C_{in} is the inlet or ambient air odorant concentration.

The uptake of odorant into the mucosa involving absorption, diffusion and removal of odorants in the nasal mucosal lining can be described to a first approximation by a dimensionless mass transfer parameter at the mucosal wall, K in several mass transport models (Hahn *et al.*, 1994; Keyhani *et al.*, 1997). The basic premise of these models is to simplify the human mucosal environment into layers of compartments: airphase, mucus, cell layer, submucosal blood compartment, etc. From these models it was possible to estimate the K-value based on the physio-chemical properties of the mucosa and odorant molecules. Based on the analysis of the steady state odorant flux through the mucosal layer, it is shown by Keyhani *et al.* (1997) that odorant gas concentration satisfies the mixed boundary condition at the mucosal wall:

$$\frac{\partial C'}{\partial y'} + KC' = 0 \text{ at } y' = 0 \quad \text{(A3)}$$

In the simplest case, K is given as

$$K = \frac{d_{in} D_m}{D_a \beta H_m} \quad \text{(A4)}$$

in which d_{in} is the hydraulic diameter (4 × area/perimeter) of the nostril, D_{m} is the odorant diffusion coefficient in mucosa, D_{a} is the odorant diffusion coefficient in air, β is the air/mucosa odorant partition coefficient ($C_{\text{a}}/C_{\text{m}}$) and H_{m} is the thickness of the mucosal layer, considered to be a constant (see Figure 9). We can obtain a reasonable estimation (Wilke–Chang equation) of D_{a} and we have some accurate experimental measurements of β for a few odorants (see Table 1) in frog mucosa, but we have only a rough estimation of D_{m} (often just the water value D_{w}) and $H_{\text{m}} = 30\ \mu\text{m}$ (Getchell *et al.*, 1984). The accuracy of the steady state mucosal model and the parameters used to produce K are limited due to our limited knowledge of the details of odorant transport in the nasal mucosa. A few of the uncertainties include: (i) increase in length of the effective diffusion path due to variations in composition of the mucosa and dense epithelial ciliary matrix, (ii) decrease in odorant diffusivity in mucus due to higher mucus viscosity and (iii) possible interaction of odorants with odorant binding proteins and other chemicals or biological agents. There has been ongoing investigation (Newton *et al.*, 2000) of the accuracy of K-values of a number of odorants by comparison of mucosa odorant uptake model with experimental odorant uptake measurement. As more information relevant to these features becomes available, the accuracy of the mucosal odorant transport model can and will be improved.

Solution method

Fluent employs a finite-volume scheme that discretizes the integral form of the governing equations for the whole computation domain into each element. An implicit second order up-winding discretization scheme is used for the convection terms and an implicit second order scheme for the viscous and diffusion terms. For the rest of the terms, a first order discretization scheme is applied. The assembly of all the elements creates a large linearized matrix which is solved iteratively by a segregated solver. Under this approach, the governing equations (continuity, NS, diffusion and convection) are solved sequentially (i.e. segregated from each other), resulting in a smaller matrix to be solved each time with less memory requirement. The segregated solver uses under-relaxation factors to control the update of each computed variable (velocity, pressure or odorant concentration, etc.) at each iteration. Default values of the under-relaxation factors are first used and then fine tuned for best convergence rate. The iterations are terminated once the convergence criterion is reached: the mean square norm of the solution vector of all unknowns changes <0.1% after an iteration.

Various mass balance conditions (e.g. volume of air flow into both nostrils equals air flow volume out the nasal pharynx, etc.) are checked to ensure a proper convergence.

Air flow and odorant flux calculations

To determine air flow rate across a given plane, such as the external naris plane, we integrate the normal velocity component over the specific surface area:

$$Q_A = \iint_A \vec{n} \cdot \vec{v} dA \quad \text{(A5)}$$

The solution of the mass transport equation (A2)–(A4) gives the concentration field of odorant in the nasal cavity. The wall mass flux j (kg/m^2) at any point on the surface of the mesh is given by the diffusive flux at the wall:

$$j = -D_a \frac{\partial C}{\partial y}\bigg|_{y=0} = \frac{D_m}{\beta H_m} C \bigg|_{y=0} \quad \text{(A6)}$$

The total flux, J (g/s), over a given surface, such as the olfactory mucosa or the entire mucosal surface is determined by surface integration of equation (A6) over the area:

$$J_A = \iint_A j \cdot \vec{n} dA \quad \text{(A7)}$$

Fractional uptake ($\eta = J_A/J_{\text{external naris}}$) is the fraction of inhaled odorant mass absorbed over a given mucosal region normalized by total inhaled odorant mass. Since the wall boundary condition (equation A4) for the mass transport equation is linear and homogeneous, the flux at every point on the nasal surface is linear with inlet concentration and fractional uptake over a given region is independent of the inlet concentration, under the assumption that the ambient odorant concentration is low and uncoupled from the air flow equation (an excellent assumption for most odorant flows). We only present odorant fractional uptake values in this paper.

Acknowledgements

The authors wish to thank Dr Dan Kurtz, SUNY Syracuse, Dr David Rosen and Dr Scott Enochs, Thomas Jefferson University, Philadelphia for their help in CT imaging and nasal airway anatomy, Dr Michael Damm and Dr Thomas Hummel, University of Dresden, Germany for their work presented at AchemS, 2002 and Dr Keyvan Keyhani for his advice in CFD analysis. This study was supported by NIH grant NIH-P50 DC 00214.

References

Abraham, M.H. and **Weathersby, P.K.** (1994) *Hydrogen bonding. 30. Solubility of gases and vapors in biological liquids and tissues*. J. Pharmacol. Sci., 83, 1450–1456.

Abraham, M.H., Kamlet, M.J., Taft, R.W., Doherty, R.M. and **Weathersby, P.K.** (1985) *Solubility properties in polymers and biological media. 2. The correlation and prediction of the solubilities of nonelectrolytes in biological tissues and fluids*. J. Med. Chem., 28, 865–870.

Damm, M., Vent, J., Schmidt, M., Theissen, P., Eckel, H., Lötsch, J. and **Hummel, T.** (2002) *Intranasal volume and olfactory function*. Chem. Senses, 27, 831–839.

Feron, F., Perry, C., McGrath, J.J. and **Mackay-Sim, A.** (1998) *New techniques for biopsy and culture of human olfactory epithelial neurons*. Arch. Otolaryngol. Head Neck Surg., 124, 861–866.

Fluent Inc. (1998) Fluent User Guide. Fluent, Lebanon, NH.

Getchell, T.V., Margolis, T.V. and **Getchell, M.L.** (1984) *Perireceptor and receptor events in vertebrate olfaction*. Prog. Neurobiol., 23, 317–345.

Girardin, M., Bilgen, E. and **Arbour, P.** (1983) *Experimental study of velocity fields in a human nasal fossa by laser anemometry*. Ann. Otol. Rhinol. Laryngol., 92, 231–236.

Hahn, I., Scherer, P.W. and **Mozell, M.M.** (1993) *Velocity profiles measured for airflow through a large-scale model of the human nasal cavity*. Modeling Physiol., 75, 2273–2287.

Hahn, I., Scherer, P.W. and **Mozell, M.M.** (1994) *A mass transport model of olfaction*. J. Theor. Biol., 167, 115–128.

Haight, J.J. and **Cole, P.** (1984) *Reciprocating nasal airflow resistances*. Acta Otolaryngol., 97, 93–98.

Hornung, D.E. and **Mozell, M.M.** (1981) *Accessibility of odorant molecules to the receptors.* In Cagan, R.H. and Kare, M.R. (eds), Biochemistry of Taste and Olfaction. Academic Press, New York, pp. 33–45.

Hornung, D.E., Mozell, M.M. and **Serio, J.A.** (1980) *Olfactory mucus/air partitioning of odorant.* In van der Starre, H. (ed.), Olfaction and Taste VII. IRL Press, London, pp. 167–170.

Hornung, D.E., Leopold, D.A., Youngentob, S.L., Sheehe, P.R., Gagne, G.M., Thomas, F.D. and **Mozell, M.M.** (1987) *Airflow patterns in a human nasal model*. Arch. Otolaryngol. Head Neck Surg., 113, 169–172.

Hornung, D.E., Smith, D.J., Kurtz, D.B., White, T. and **Leopold, D.A.** (2001) *Effect of nasal dilaors on nasal structures, sniffing strategies, and olfactory ability*. Rhinology, 39, 84–87.

Kelly, J.T., Prasad, A.K. and **Wexler, A.S.** (2000) *Detailed flow patterns in the nasal cavity*. J. Appl. Physiol., 89, 323–337.

Keyhani, K., Scherer, P.W. and **Mozell, M.M.** (1995) *Numerical simulation of airflow in the human nasal cavity*. J. Biomech. Eng., 117, 429–441.

Keyhani, K., Scherer, P.W. and **Mozell, M.M.** (1997) *A numerical model of nasal odorant transport for the analysis of human olfaction*. J. Theor. Biol., 186, 279–301.

Leopold, D.A. (1988) *The relationship between nasal anatomy and human olfaction*. Laryngoscope, 98, 1232–1238.

Martonen, T.B., Quan, L., Zhang, Z. and **Musante, C.J.** (2002) *Flow simulation in the human upper respiratory tract*. Cell Biochem. Biophys., 37, 27–36.

Masing, H. (1967) *Experimental studies on the flow in nose model*. Arch. Klin. Exp. Ohren Nasen Kehlkopfheilkd., 189, 59–70.

Moulton, D.G. (1976) *Spatial patterning of response to odors in the peripheral olfactory system*. Physiol. Rev., 56, 578–593.

Mozell, M.M. (1966) *The spatiotemporal analysis of odorants at the level of the olfactory receptor sheet*. J. Gen. Physiol., 50, 25–41.

Mozell, M.M. (1970) *Evidence for a chromatographic model of olfaction*. J. Gen. Physiol., 56, 46–63.

Mozell, M.M. and **Jagodowicz, M.** (1974) *Mechanisms underlying the analysis of odorant quality at the level of the olfactory mucosa. I. Spatiotemporal sorption patterns*. Ann. N. Y. Acad. Sci., 237, 76–90.

Newton, J.W., Zhao, K., Hornung, D.E. and **Kurtz, D.B.** (2000) *Determination of odorant solubility in the olfactory mucosa*. Chem. Senses, 25, 609–609.

Pallanch, J.F., McCaffrey, T.V. and **Kern, E.B.** (1985) *Normal nasal resistance*. Arch. Otolaryngol. Head Neck Surg., 93, 778–785.

Perry, R.H., Chilton, C.H. and **Kirkpatrick, S.D.** (1963) Chemical Engineers' Handbook. McGraw-Hill, New York.

Pribitkin, E.D., Cowart, B.J., Rosen, D., and **Klock, C.T.** (2003) *Prognosis for olfactory dysfunction: the good, the bad, and the ugly [abstract]*. Chem. Senses, 28, 000.

Proctor, D.F. (1982) *The upper airway.* In Proctor, D.F. and Andersen, I.B. (eds), The Nose. Elsevier Biomedical, New York, pp. 23–43.

Proetz, A.W. (1951) *Air currents in the upper respiratory tract and their clinical importance*. Ann. Otol. Rhinol. Laryngol., 60, 439–467.

Schreck, S., Sullivan, K.J., Ho, C.M. and **Chang, H.K.** (1993) *Correlations between flow resistance and geometry in a model of the human nose*. J. Appl. Physiol., 75, 1767–1775.

Stuiver, M. (1958) Biophysics of the Sense of Smell. Dissertation, Rijks University, Groningen, The Netherlands.

Subramaniam, R.P., Richardson, R.B., Morgan, K.T. and **Kimbell, J.S.** (1999) *Computational fluid dynamics simulations of inspiratory airflow in the human nose and nasopharynx*. Inhal. Toxicol., 10, 91–120.

Swift, D.L. and **Proctor, D.F.** (1977) *Access of air to the respiratory tract.* In Brain, J.D., Proctor, D.F. and Reid, L.M. (eds), Respiratory Defense Mechanism. Marcel Dekker, New York, pp. 63–91.

Welty, J.R., Wicks, G.E. and **Wilson, R.E.** (1976) Fundamentals of Momentum, Heat and Mass Transfer, 2nd edn. Wiley, New York.

Wolfensberger, M. and **Hummel, T.** (2002) *Anti-inflammatory and surgical therapy of olfactory disorders related to sino-nasal disease*. Chem. Senses, 27, 617–622.

Accepted February 24, 2004